Novel hybrid laser forging and arc additive repairing process for improving component performances

Yongkang Zhang[1,2,3], Dongsheng Wu[4]*, Dihui Xie[1], Hebin Wu[3], Chaohui Lin[1,3], Qi Zhang[1], Jinlong Ke[1], Guibin Tan[1,2], Ninshu Ma[4], Yanbing Guo[5]

1. School of Electromechanical Engineering, Guangdong University of Technology, Guangzhou, 510006, PR China
2. Guangdong Provincial Key Laboratory of Advanced Manufacturing Technology for Marine Energy Facilities, Guangdong University of Technology, Guangzhou, 510006, China
3. State Key Laboratory of Precision Electronic Manufacturing Technology and Equipment, Guangdong University of Technology, Guangzhou 510006, PR China
4. Joining and Welding Research Institute (JWRI), Osaka University, 11-1 Mihogaoka, Ibaraki, Osaka 567-0047, Japan
5. College of Ocean Science and Engineering, Institute of Marine Materials Science and Engineering, Shanghai Maritime University, Shanghai, 201306, China

* Corresponding author, Email address: d.wu@jwri.osaka-u.ac.jp

Abstract

A new hybrid laser forging and arc additive repairing process was developed to significantly improve the performance of repaired components, in which a leading gas metal arc was adopted to repair the partially damaged component, and a trailing short-pulse laser directly acted on the high-temperature solidified metal without coating (laser forging). Compared with arc additive repairing with post-treatment, this hybrid process performed the arc repair and laser forging synchronously. The laser forging region can be accurately determined using a multi-physical molten pool simulation. The molten metal flow was also studied, indicating that the high sulfur content introduced by the filler metal transfer had a significant influence on the Marangoni stress distribution and thus changed the molten metal flow patterns. The mechanism for laser forging without coating and its related physical effects were investigated. The laser shock pressure was significantly higher than the Hugonoit elastic limit of the high-temperature solidified metal, causing plastic deformation of the repaired layer. The high strain and severe plastic deformation induced by laser forging caused martensite formation and grain refinement, which improved the mechanical properties and electrochemical corrosion performance of the repaired layer.

Keywords: hybrid laser forging and arc additive repairing process, laser forging, laser peening, multi-physical simulation, martensite transformation

1 Introduction

Failures caused by stress corrosion [1], electrochemical corrosion [2], friction and wear [3], and fatigue [4] are the main causes of component failures in aerospace, marine, petrochemical, rail transit, and wind power industries. Arc additive repairing of partially damaged components could extend the lifetime of the components and reduce the manufacturing cost [5, 6]. Conventional methods such as stress relief annealing [7], cold rolling [8] and shot peening [9] are adopted as post treatments to improve the performance of repaired components.

Laser shock peening (LSP) [10,11] is an effective and non-destructive surface modification technique that can introduce deeper and higher compressive residual stress and obtain better component performance compared with conventional post-treatment techniques. A schematic of LSP as a post-treatment technique is shown in **Fig. 1(a)**. After the repair, the repaired region is covered by two layers: absorbing and confining layers. When a laser pulse (tens of nanoseconds) with a high energy density (GW/cm^2) hits the surface of the absorbing layer, the absorbing layer vaporizes, generating plasma [12]. The plasma continues to absorb the laser energy and rapidly expands. The plasma is trapped between the absorbing and confining layers, creating a high surface pressure (on the order of gigapascals). The surface pressure propagates into the repaired layer as a shockwave [13] and produces plastic deformation in the surface layer of the repaired region. The maximum compressive stress and influence depth can be several hundred Mpa and 1 mm, respectively [14, 15]. Chattopadhyay et al. [16] proposed that strain hardening and changes in the microstructure caused by LSP led to significant improvements in the tensile and fatigue properties of a pure titanium weldment. Chen et al. [17] found that after LSP, the grains were significantly refined and high-level compressive residual stresses were introduced into an Incoloy 800H weldment. Kalentics et al. [18, 19] showed that LSP as a post-treatment technique could suppress cracks and improve the fatigue properties of selective laser-melted parts. However, LSP as a post-treatment technique is complicated and its efficiency is low, making it difficult to act on a multi-layer and multi-pass repaired component.

A new hybrid laser forging and arc additive repair process was developed to significantly improve the performance of the repaired component. As shown in **Fig. 1(b)**, in this process, a leading gas metal arc (GMA) is adopted to repair the component, and without absorbing and confining layers, a trailing short-pulse laser with high energy density directly acts on the high-temperature solidified metal (direct ablation), inducing metal evaporation and ionization. A shockwave was generated and propagated into the metal. The plastic deformation of the high-temperature solidified metal occurs easily (laser forging). Note that the hybrid laser forging and arc additive repairing processes differ from LSP as a post-treatment technique. In this hybrid process, arc repair and laser forging are performed synchronously,

and the laser beam directly acts on the high-temperature solidified metal without coating, changing the microstructure, residual stress distribution, and component performance. Previous studies showed that the hybrid wire arc additive manufacturing and shot peening process can relief the residual stress and minimize distortion [20], and hybrid laser directed energy deposition and shot peening process can effectively improve the mechanical properties of formed materials [21]. As a new hybrid process, the laser forging mechanism and its related physical effects have not yet been revealed.

In this study, a hybrid laser forging and arc additive repair process was developed to improve the performance of the Q460 steel component used in offshore wind power platforms. In order to accurately determine the laser forging region, a multi-physical numerical model considering filler metal transfer and molten pool convection was developed. The molten metal flow was also studied. The microstructure, mechanical properties, and electrochemical corrosion performance of the repaired layers were investigated. The laser forging mechanism and its effects on the performance of the repaired layer were revealed.

2 Experiment procedures

Fig. 1(b) shows a schematic of the hybrid laser forging and arc additive repair processes. Q460 low-alloy high-strength steel plates with a thickness of 15 mm were adopted as the substrate, and a groove was used to represent the removed damage region, as shown in **Fig. 1(c)**. To clearly reveal the effects of laser forging on the repaired layer performance, both one-pass arc additive repair and one-pass hybrid laser forging and arc additive repair processes were performed.

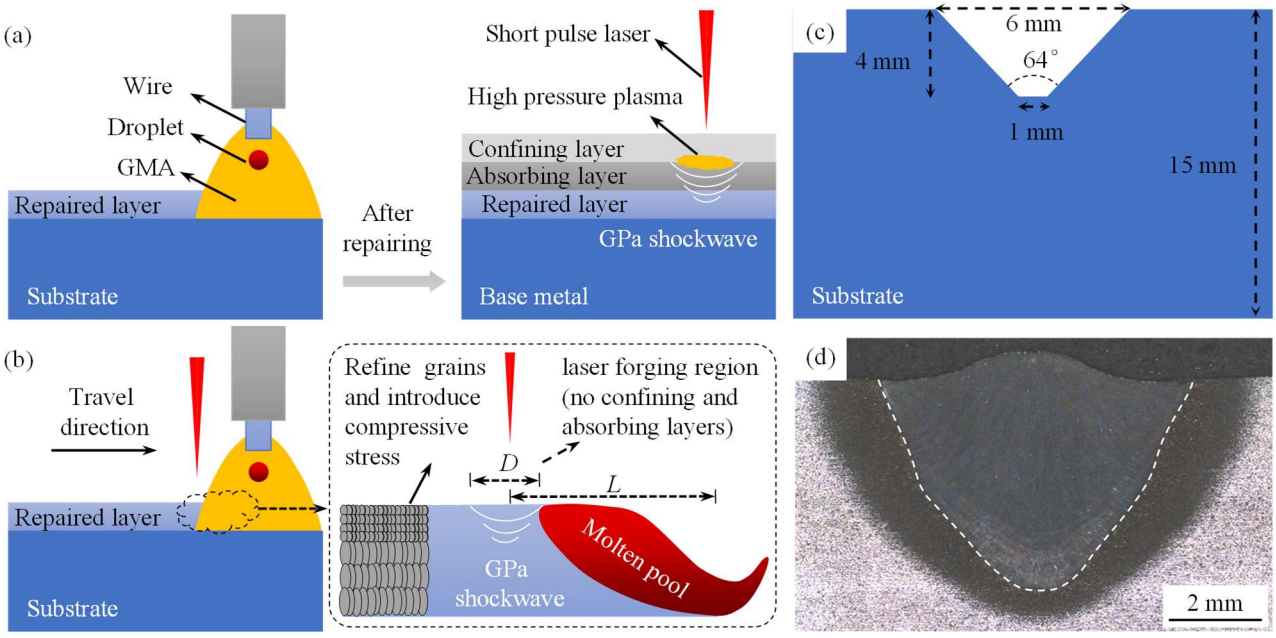

Fig.1 (a) Schematic of LSP as a post treatment technique; (b) Schematic of the hybrid process; (c) Groove shape; (d) Cross-sectional photograph of the repaired layer made by the hybrid process

A leading GMA was used to repair the Q460 substrate, and an MFR-500 welding machine was used as the power source. Pure argon was used as a shielding gas. An ER110S-G wire with a diameter of 1.2 mm was used as the filler metal. A trailing short-pulse laser (using a Q-switched Nd:YAG laser with a wavelength of 1064 nm, diameter of 4 mm (D)) directly acted on the high-temperature solidified metal without a coating. The region directly impacted by the laser was defined as the laser-forging region. Based on the calculated temperature distribution from a multi-physical molten pool simulation, the distance between the laser beam center and welding torch center (L) was set to approximately 10 mm, and a laser forging region with a diameter of 4 mm was determined.

The detailed process parameters can be seen in **Table. 1**, and the compositions of Q460 steel and ER110S-G wires are listed in **Table. 2**.

Table.1 Detailed processing parameters

Arc current	Arc voltage	Gas rate	Travel speed	Laser frequency	Pulse energy	Pulse duration
160 A	24 V	20 L/min	0.45 m/min	10 HZ	1 J	6 ns

Table.2 Compositions of the Q460 steel and ER110S-G wire (wt%)

	C	Mn	Si	P	S	Cr	V	Cu	Ni	Mo	Ti
Q460	0.16	0.98	0.38	0.02	0.003	0.03	0.05	0.21	0.02	-	-
ER110S-G	0.06	1.68	0.52	0.01	0.013	0.03	-	0.17	0.54	0.34	0.06

After the repair processes, metallographic samples were extracted from the cross-section of the repaired layer, then polished, and etched using a 4% nitric acid ethanol solution for 4–6 s at room temperature. Macrostructures of the metallographic samples were observed using an OLYMPUS laser confocal microscope. Laser forging has a minor influence on the formation of the repaired layer, and a cross-sectional photograph of the repaired layer made by the hybrid process is shown in **Fig. 1(d)**. The microstructures were observed using an optical microscope (OM; Zeiss Primotech). Tensile tests were performed using a GHS50K universal testing machine at a constant speed of 2 mm/min, following the GB/T2651-2008 standard. The fracture morphologies of the tensile samples were observed using scanning electron microscopy (SEM, S-3400N). The electrochemical corrosion tests were conducted using an electrochemical system (CHI660E) with a standard three-electrode cell in a 3.5% NaCl solution at room temperature. Electrochemical impedance spectroscopy (EIS) and potentiodynamic polarization tests were performed to evaluate the corrosion behavior.

3 Multi-physical model

Multi-physical phenomena, such as filler metal transfer, molten pool surface deformation, and molten metal convection, are considered in the numerical model to accurately predict the dynamic molten pool behaviors and determine the laser forging region. A computational domain with dimensions of 35 mm x 30 mm x 18 mm was defined, as shown in **Fig. 2(a)**. A base metal region with

a groove was predefined at the bottom of the computational domain, and the other region was set as a void. The height of the base metal region was 15 mm. Nonuniform hexahedral mesh grids were adopted: finer mesh grids (0.2 mm) were used for the region near the repaired layer, and coarser mesh grids were used for other regions.

The governing equations of the multi-physical molten pool simulation involve the species, mass, momentum, and energy conservation equations and the volume of fluid (VOF) equation. The GMA dynamics were ignored, while the GMA heat source, arc pressure, and shear stress were applied to the free surface of the molten pool. The liquid metal was considered to be an incompressible Newtonian fluid, and the flow was laminar. The short-pulse laser directly acted on the high-temperature solidified metal, not the molten pool. Besides, the pulse duration was only 6 ns, therefore the heat effect of the laser was not considered in the molten pool model. The mass, momentum, energy conservation, and VOF equations can be found in our previous study [22]. Here, the species conservation equation, arc heat source, arc pressure, shear stress, surface tension, Lorentz force, and boundary conditions are described. The commercial software FLOW3D with programming language Fortran is used to solve the governing equations.

3.1 Specie conservation equation

The conservation of the sulfur element was considered, in which the diffusive effect of sulfur was ignored [23]:

$$\frac{\partial(\rho\varphi)}{\partial t} + \nabla \cdot (\rho \boldsymbol{v} \varphi) = \varphi_s \tag{1}$$

The sulfur content of the base metal was 0.003%. Spherical drops with a specific height, radius, velocity, frequency, temperature, and sulfur content are introduced to approximate the filler metal transfer. The sulfur content was set to 0.013% for each droplet.

3.2 Heat source and forces models

The GMA heat source (q_{arc}) acting on the top molten pool surface was modeled as a fixed Gaussian density function [24]:

$$q_{arc} = \frac{\eta_q U_q I_q}{2\pi\sigma_r} \exp\left\{-\frac{(x-x_0-v_w t)^2+y^2}{2{\sigma_r}^2}\right\} \tag{2}$$

Previous studies showed the total energy efficiency of GMA welding process was about 68%~78% [25,26]. In this study, the total energy efficiency 75% was adopted for the GMA.

The arc pressure (P_{arc}) and shear stress ($\boldsymbol{\tau_G}$) distributions obtained from the arc model are shown in **Fig. 2(b)**. The surface tension of the molten metal is considered a function of temperature and sulfur content [27]. The high sulfur content introduced by filler metal transfer has a significant influence on the surface tension.

$$\gamma(T) = \gamma_m^0 - A(T - T_m) - \mathrm{R}T\Gamma_s ln\left(1 + K_l \alpha_s e^{(-\Delta H_0/RT)}\right) \tag{3}$$

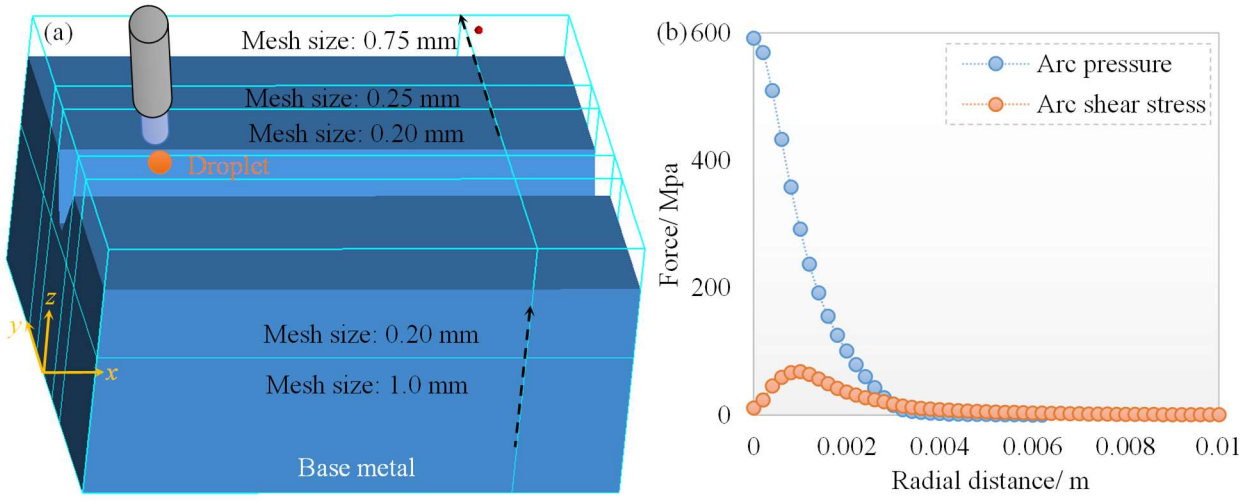

Fig.2 (a) Computational domain; (b) Arc pressure and shear stress distributions

The Lorentz force is calculated as below [28]:

$$F_x = -J_z \times B_\theta \frac{x - x_0 - v_w t}{\sigma_r} \tag{4}$$

$$F_y = -J_z \times B_\theta \frac{y}{\sigma_r} \tag{5}$$

$$F_z = -J_r \times B_\theta \tag{6}$$

The symbols and nomenclature are listed in **Table. 3**.

Table.3 Symbols and nomenclature

Symbol	Nomenclature	Symbol	Nomenclature
ρ/ (Kg.m^{-3})	Density	φ/ wt%	Weight percentage of sulfur
t/ s	Time	$\boldsymbol{v}$/ (m.s^{-1})	Velocity vector
φ_s/ (wt%.Kg. m^{-3}.s^{-1})	Sulfur source term caused by the filler metal transfer.	η_q	GMA energy efficiency
U_q/ V	GMA voltage	I_q/ A	GMA current
σ_r/ m	Gaussian distribution parameter	x_0/ m	Original torch location
v_w/ (m.s^{-1})	Travel speed	γ_m^0/ (N. m^{-1})	Surface tension of the pure metal at the melting point
A/ / (N. m^{-1}.K^{-1})	Negative of surface tension gradient for the pure metal	T/ K	Molten temperature
T_m/ K	Melting point	R/ (J.K^{-1}.mol^{-1})	Gas constant
Γ_s/ (Kg.mol.m^{-2})	Surface excess at saturation	K_l	Entropy factor
α_s/ wt%	Sulfur content	ΔH_0/ (J.mol^{-1})	Heat of absorption
F_x, F_y, and F_z/ (N.m^{-3})	Components of the Lorentz force in x, y, and z directions	J_z/ (A.m^{-2})	Axial component of the current density
J_r/ (A.m^{-2})	Radial component of the current density	B_θ/ (N. A^{-1}.m^{-1})	Angular component of the magnetic field

3.3 Material properties

The alloying element contents of Q460 steel and ER110S-G wire were not significantly different. In the simulation, it was assumed that the thermophysical material properties of Q460 steel and ER110S-G wire were the same. The specific heat, thermal conductivity, and density can be seen in **Fig. 3,** and other material properties are shown in **Table. 4** [29].

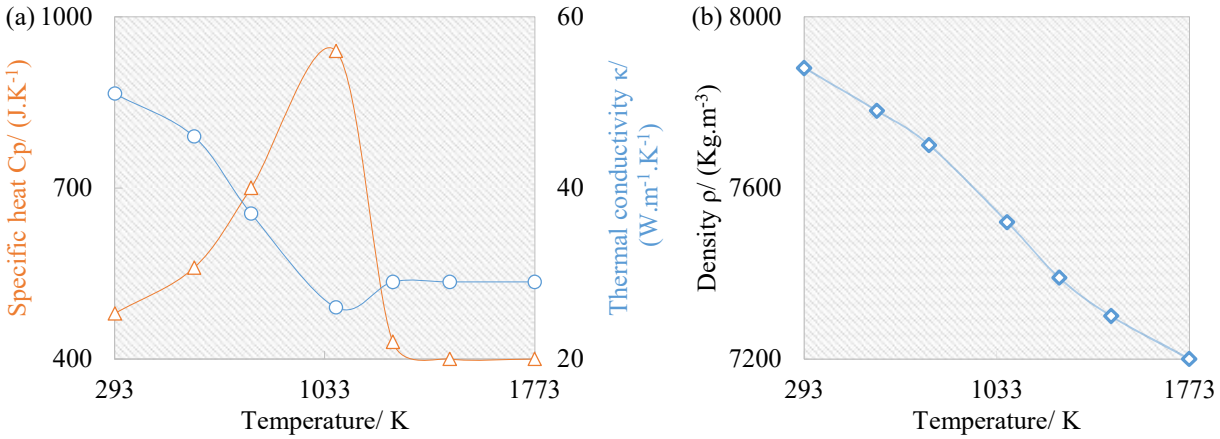

Fig. 3 Thermo-physical material properties of the Q460 steel: (a) Specific heat and thermal conductivity; (b) Density

Table. 4 Thermo-physical material properties of the Q460 steel

Viscosity / $Kg.m^{-1}.s^{-1}$	0.0059	Latent heat of fusion / $J.Kg^{-1}$	2.77e5
Melting point / K	1768	Coefficient of thermal expansion / K^{-1}	1e-5

4 Results

4.1 Molten pool behaviors

As shown in **Fig. 4**, at t = 3.0 s and in the y = 0 cross-section, the molten metal primarily flowed backward at the top surface before and after the droplet, while flowing forward at the molten pool edge. The molten metal flowed downwards inside the molten pool below the droplet and a clockwise eddy was formed. In the trailing part of the molten pool, an anticlockwise eddy was formed.

At the top surface of the x = 22.1 mm cross-section, the molten metal mainly flowed upward and inward from the pool edge to the pool center. The molten metal flowed downward inside the molten pool. At the top surface of the x = 25.1 mm cross-section, the molten metal primarily flowed downwards and inward from the pool edge to the pool center. The molten metal flowed upward inside the molten pool. At the pool edge of the x = 27.3 mm cross-section, the molten metal mainly flows downwards and inward. In the pool center, the molten metal flowed upward in the top part and downwards in the bottom part.

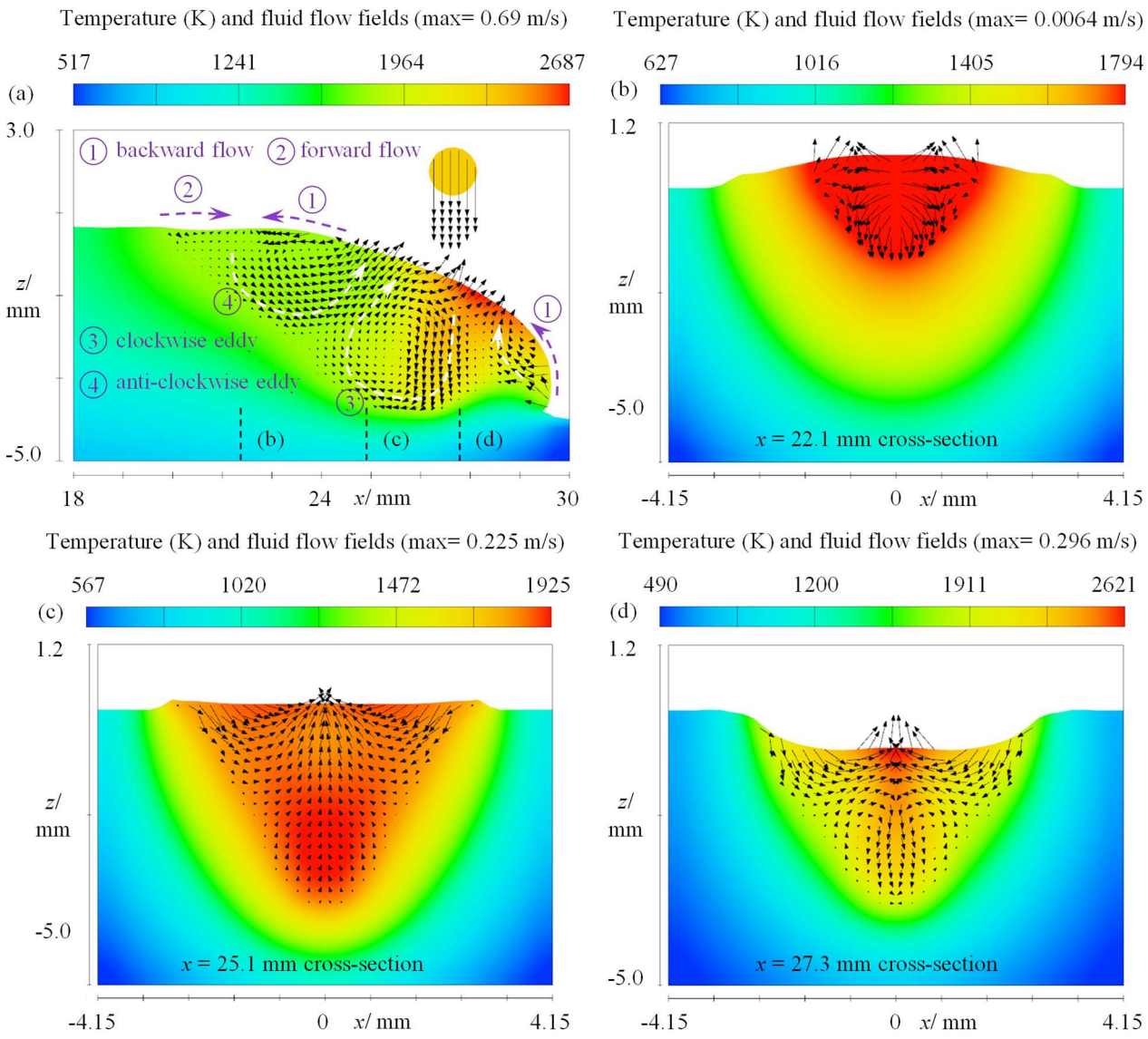

Fig. 4 Temperature and fluid flow fields at t = 3s: (a) y = 0 cross-section; (b) x = 22.1 mm cross-section; (c) x = 25.1 mm cross-section; (d) x = 27.3 mm cross-section

The three-dimensional temperature and fluid flow fields at t = 3s are shown in **Fig. 5(a)**. A teardrop-shaped molten pool was formed. The molten metal mainly flows inward in the center region of the molten pool and backward in the trailing part. Comparisons between the calculated and experimentally repaired layer geometries are shown in **Fig. 5(b)**. The experimental repaired layer width and depth were 6.77 mm and 4.43 mm, respectively. The calculated repaired layer width and depth are 7.03 mm and 4.06 mm respectively, which agree well with the experimental results.

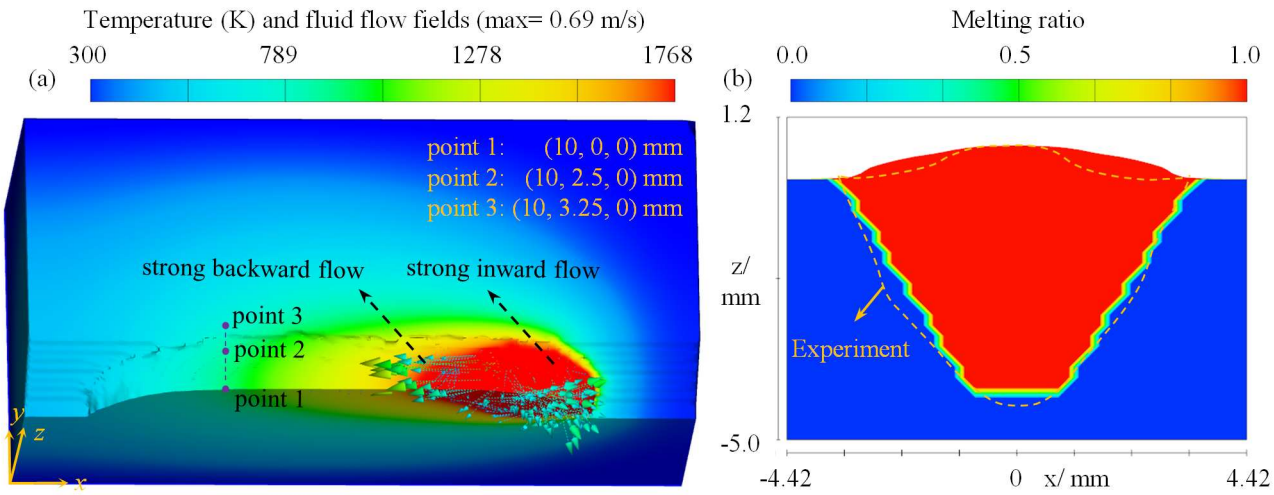

Fig. 5 (a) Three-dimensional temperature and fluid flow fields at t = 3s; (b) Comparisons between calculated and experimental repaired layer geometries

The temperature vs. time plots of the three points (as shown in **Fig. 5(a)**, their locations are (10, 0, 0) mm, (10, 2.5, 0) mm, and (10, 3.25, 0) mm, respectively) are shown in **Fig. 6(a)**. Point 1 was located at the pool center. The molten temperature of point 1 reaches a maximum value of 2269.8 K at t = 0.78 s, and rapidly decreases to 1797 K at t = 0.975 s. As shown in **Fig. 6(b)**, the molten metal of point 1 slowly solidifies from 1797 K to 1768 K at an average cooling rate of 56.9 K/s; after the solidification, the temperature of point 1 quickly decreases to 830.2 K at t = 3.0 s at an average cooling rate of 625.2 K/s. Point 2 was located at the pool edge, and the maximum molten temperature was only 1797.3 K. The molten metal of point 2 solidifies from 1797 K to 1768 K at a high average cooling rate of 122.3 K/s; after the solidification, the temperature of point 2 decreases to 758.9 K at t = 3.0 s at a low average cooling rate of 487.5 K/s. Point 3 is located at the heat-affected zone (HAZ); here, the temperature increases slowly to 1229.4 K at t = 0.975 s, and then decreases to 705.3 K at t = 3.0 s.

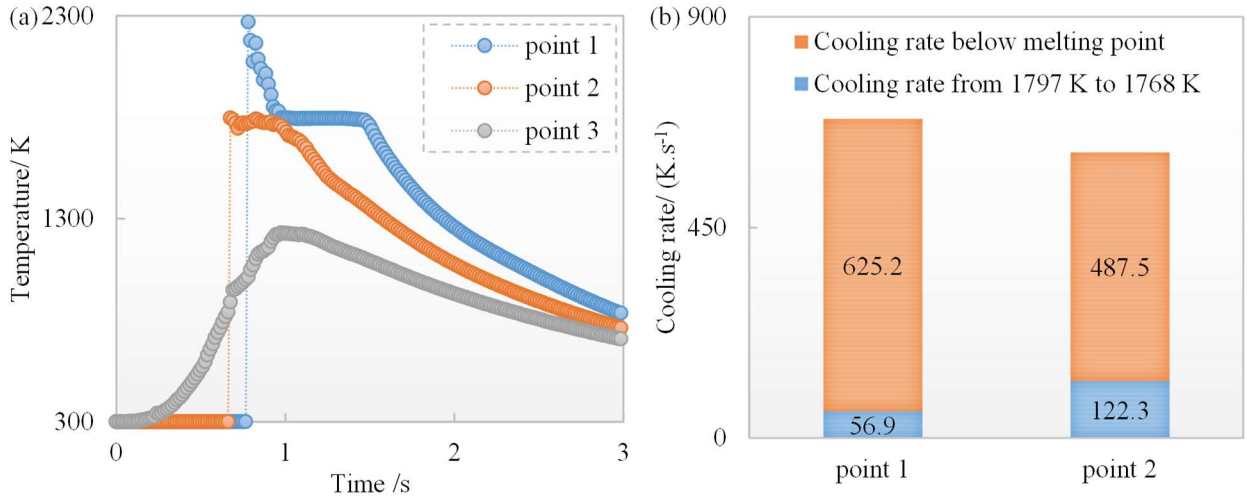

Fig. 6 (a) Temperature vs time plot of three points; (b) Cooling rates of two points

4.2 Microstructures of the repaired layers

As shown in **Fig. 7**, the microstructure of Q460 steel consists of ferrite (F) and pearlite (P), in which pearlite clusters are distributed discontinuously in the ferrite. The microstructure of the fusion zone in the arc additive repair process mainly consists of polygonal ferrite (PF) with a small amount of acicular ferrite (AF), with a ferrite size of approximately 1.6 ~6.4 μm. The microstructure of the fusion zone in the hybrid laser forging and arc additive repair process mainly consists of fine acicular ferrite with a small amount of martensite (M), and the ferrite size is approximately 1.2 ~2.4 μm.

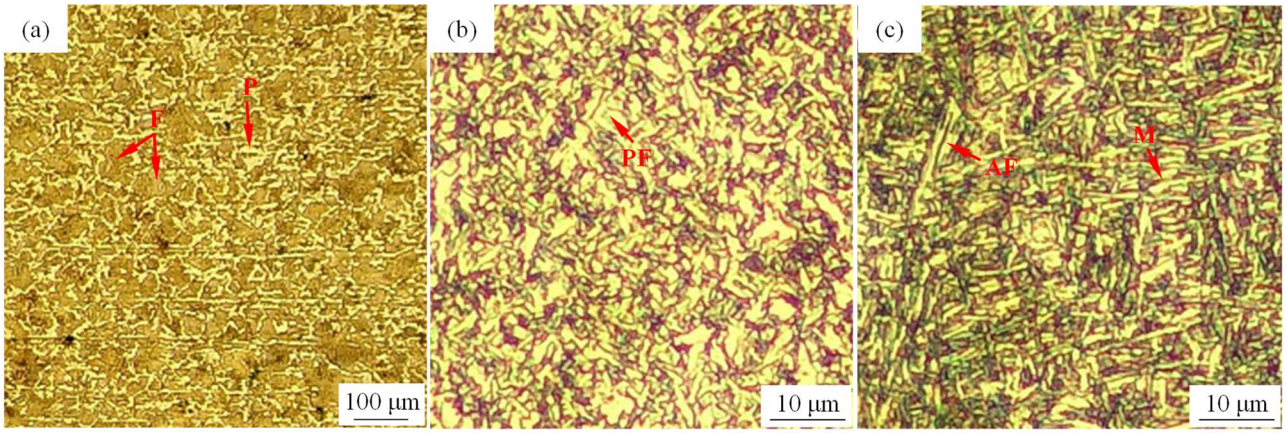

Fig. 7 Microstructure of (a) Q460 steel; (b) Fusion zone of the arc additive repairing process; (c) Fusion zone of the hybrid laser forging and arc additive repairing process

In the HAZ, the cooling rate was lower than that in the fusion zone. As shown in **Fig. 8 (a)** and **(b)**, in both the arc additive repair and hybrid laser forging and arc additive repair processes, the HAZs contain coarse martensite, acicular bainite (B), and retained austenite (RA). Laser forging has a minor influence on the microstructure of the HAZ.

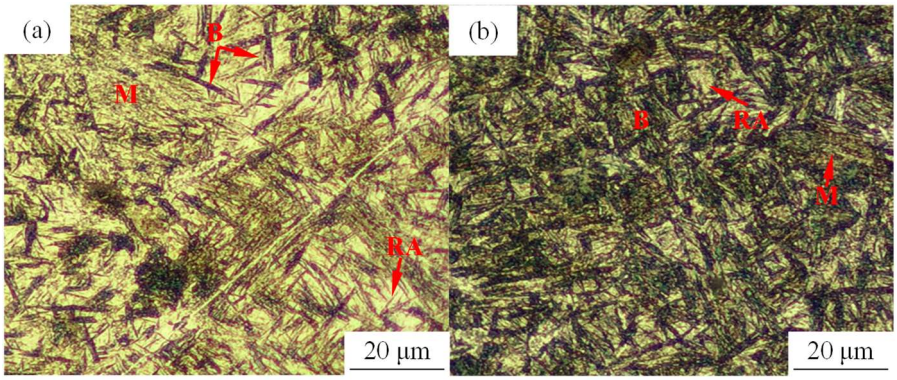

Fig. 8 Microstructure of the HAZ: (a) Arc additive repairing process; (b) Hybrid laser forging and arc additive repairing process

4.3 Performances of the repaired layers

As shown in **Fig. 9**, the tensile strength of the repaired layer made by the arc additive repair process was 590 MPa, and the elongation was 6.05%. In addition, the tensile specimen fractured in the fusion zone. The tensile strength of the repaired layer made by the hybrid laser forging and arc additive repairing process was 683 MPa, and the elongation is 9.54%; the tensile strength and elongation were

improved by 15.76 % and 57.69%, respectively. The experimental repaired layer width was 6.77 mm, while the diameter of the short-pulse laser was only 4 mm. As a result, laser forging affected the fusion zone, but had a minor influence on the microstructure of the HAZ, and the forged specimen fractured in the HAZ.

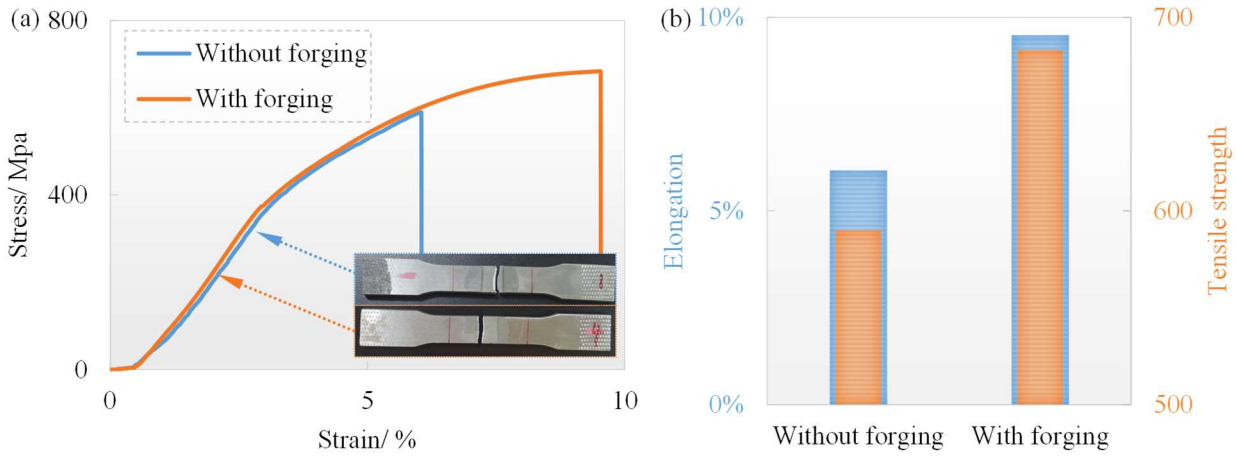

Fig. 9 (a) Tensile stress-strain curve; (b) Tensile strength and elongation

Fig. 10 shows the SEM tensile fracture morphologies of the specimens. Smooth cleavage planes and torn edges can be clearly observed on the fracture surface in the arc additive repairing process. These features are the typical characteristics of the intergranular fracture mode. The fracture surface in the hybrid laser forging and arc additive repairing process shows a large amount of dimples accompanied by a few cleavage planes, torn edges and secondary cracks, indicating the fracture mechanism is a mixture of ductile and cleavage fractures after laser forging.

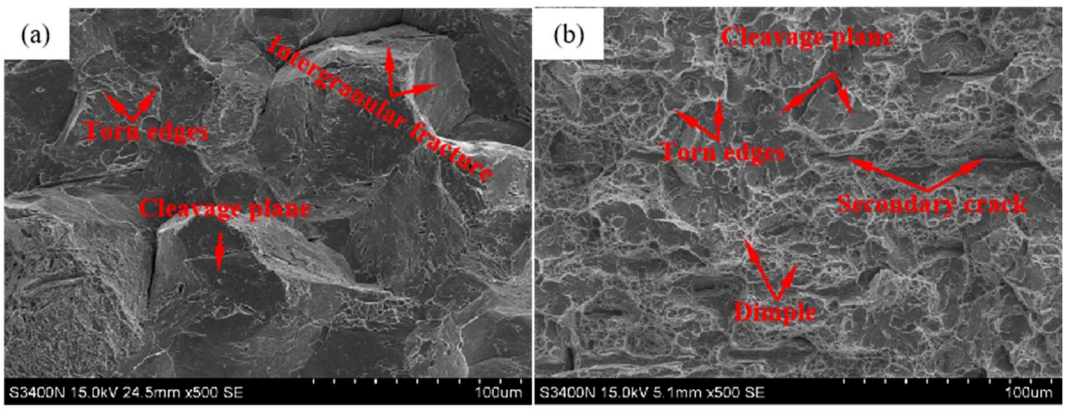

Fig. 10 Tensile fracture morphologies: (a) arc additive repairing process; (b) Hybrid laser forging and arc additive repairing process

Fig. 11(a) describes the potentiodynamic polarization curves. All detected curves have the characteristics of the passivation phenomenon with obvious passivation ranges, indicating passive films are formed on the specimen surfaces. For the specimen of the arc additive repairing process, the self-corrosion potential and corrosion current are -0.651 V and 8.141 e-6 A, respectively. For the

specimen of the hybrid laser forging and arc additive repairing process, the polarization curve moves to the right, approaching the positive electrode. The self-corrosion potential increases to -0.614 V, and the corrosion current decreases to 4.572 e-6 A. With forging, the self-corrosion potential increases by 5.7% and the corrosion current decreases by 43.8%, therefore, the corrosion tendency decreases. **Fig. 11(b)** describes the electrochemical impedance spectroscopy measurement results. It can be clearly seen that the capacitive arc of the specimen of the hybrid laser forging and arc additive repairing process has a larger radius, indicating a better corrosion resistance.

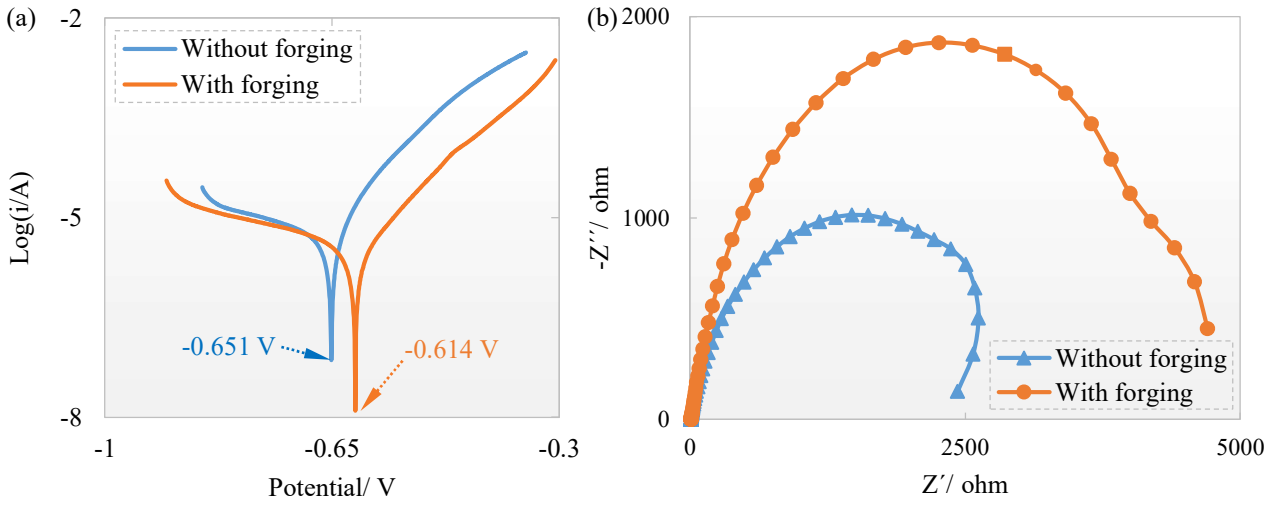

Fig. 11 (a) Potentiodynamic polarization curves; (b) Electrochemical impedance spectroscopy measurement results

Fig. 12 shows the typical corroded surfaces of these two processes. Both of them exhibit typical characteristics of pitting corrosion. There are a large number of corrosion pits on the surface of the specimen of the arc additive repairing process, and the pit area is 29.4%. The corrosion pits on the surface of the specimen of the hybrid laser forging and arc additive repairing process are reduced, and the pit area is 8.7%.

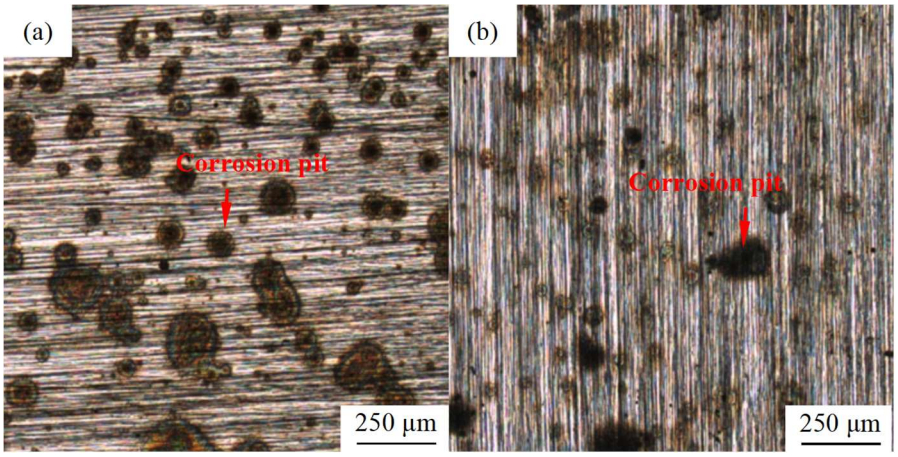

Fig. 12 Electrochemical corrosion morphologies: (a) Arc additive repairing process; (b) Hybrid laser forging and arc additive repairing process

5 Discussion

5.1 Effects of the sulfur content on the molten pool convection

Previous numerical studies on GMA welding of low-carbon steels showed that the molten metal flowed backward or outwards at the pool edge [30, 31]. However, as shown in **Fig. 4**, the molten metal flow patterns in this study are significantly different from those in the GMA welding of low-carbon steels, which is caused by the sulfur content. **Fig. 13(a)** shows the distribution of the calculated sulfur content. In the central region of the groove, the sulfur content was as high as 0.013 %; on the side of the groove, the base metal is melted and a low dilution rate can be observed. **Fig. 13(b)** shows the surface tension as a function of the temperature and sulfur content. When the sulfur content was 0.003%, the surface tension temperature gradient is mainly negative. When the sulfur content is 0.013%, the surface tension temperature gradient is positive at temperatures about lower than 2000 K and negative at the temperatures higher than 2000 K.

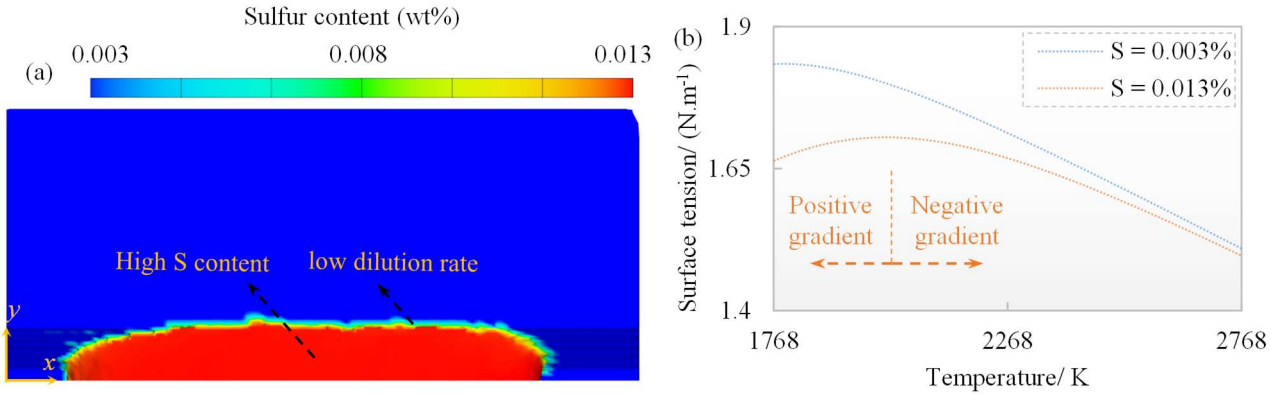

Fig. 13 (a) Calculated sulfur content; (b) Surface tension as a function of the temperature and sulfur content

The arc pressure and shear stress, Marangoni stress, Lorentz force, and droplet impact force are the dominant driving forces for molten metal flow in a GMA pool. As shown in **Fig. 14(a)**, the arc pressure acts downwards and vertically on the molten-pool surface [32]. The arc shear stress acts on the molten pool surface and promotes the outward flow of molten metal from the pool center to the pool edge [24]. At the center of the molten pool surface, the temperature is high, and the surface tension temperature gradient is negative; therefore, the Marangoni stress also promotes the outward flow of the molten metal from the pool center. However, at the trailing part of the molten pool surface, the temperature is low and the surface tension temperature gradient becomes positive; therefore, the Marangoni stress causes the molten metal to flow forward [33]. The Lorentz force causes the molten metal to flow inward and downwards below the arc center. The droplet impact force also promotes the downward flow of the molten metal [34].

As shown in **Fig. 14(b)**, it can be concluded that the backward flow at the top surface before the droplet is primarily driven by the Marangoni stress; the backward flow at the top surface after the droplet is mainly driven by the arc shear stress and Marangoni stress; the forward/inward flow in the

pool edge is primarily driven by the Marangoni stress; as the backward and forward flows collide with each other, the molten metal flows downwards, and the anti-clockwise eddy forms in the trailing part of the molten pool; the clockwise eddy is primarily driven by the arc pressure, Lorentz force, and droplet impact force.

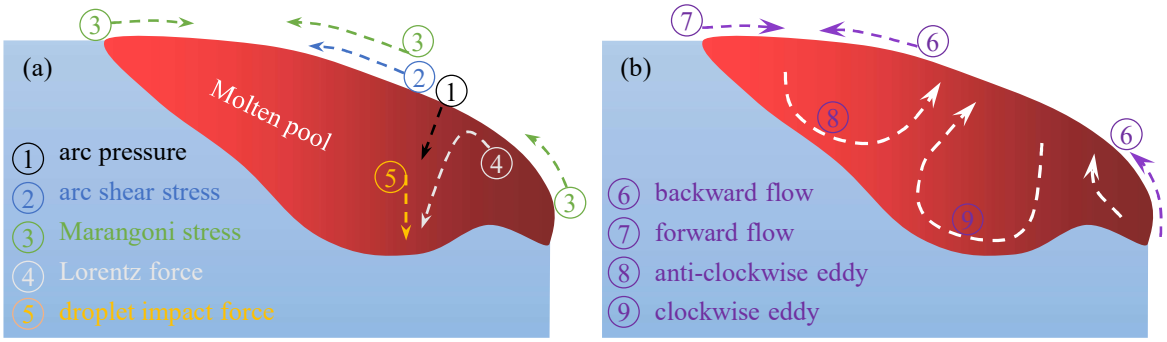

Fig. 14 Diagrams of: (a) Driven forces for the molten metal flow; (b) Molten flow patterns

5.2 Laser forging mechanism and related physical effects

For the laser peening process, the laser-matter interaction mode is "confined ablation, " in which the generated plasma is confined by a confining layer. Laser shock pressure in the "confined ablation" mode has been widely investigated [35, 36]. However, for a laser forging process, the laser-matter interaction mode is "direct ablation," in which a short-pulse laser with high energy density directly acts on the high-temperature solidified metal. Here, the laser shock pressure in the "direct ablation" mode was derived from Fabbro's study [37]. In Fabbro's model, the pressure generated by the plasma induced a shock wave that propagated into both the metallic target and confining layer. The laser shock pressure can be calculated as follows:

$$P_{max}(Mpa) = 3220 \times \left(\frac{\alpha}{2\alpha+3}\right)^{2/3} \times \rho_0^{1/3}(g/cm^3) \times I_0^{2/3}(GW/cm^2) \quad (7)$$

$$2\rho_0^{1/2} = \rho_1^{1/2} + \rho_2^{1/2} \quad (8)$$

where α is a constant fraction ($\approx$ 0.1-0.2), ρ_1 and ρ_2 are the densities of the metallic target and confining layer, respectively, and I_0 is the laser energy density.

In the hybrid laser forging and arc additive repair process, the shielding gas with a density of $\rho_3$is considered as the confining layer, as shown in **Fig. 15(a)**. ρ_0 is replaced by $4\rho_3$, and the fraction α with a large value of 0.2 is adopted; thus, the laser shock pressure in the hybrid process can be calculated as

$$P_{max}(Mpa) = 93.8 \times I_0^{2/3}(GW/cm^2) \quad (9)$$

In this work, the laser energy density I_0 is approximately 1.33 GW/cm^2, the laser shock pressure is approximately 113.4 MPa. Plastic deformation occurs when the laser shock pressure exceeds the Hugonoit elastic limit (*HEL*) of the material.

$$P_{max} \geq HEL \tag{10}$$

HEL is related to the dynamic yield strength at high strain rates. For the one-dimensional strain condition and idealized elastic–plastic material, the *HEL* can be simplified as [38]

$$HEL = (\frac{K}{2G} + \frac{2}{3})Y = \frac{1-\nu}{1-2\nu}Y \tag{11}$$

where K is the bulk modulus, G is the shear modulus, ν is the Poisson's ratio, and Y is the yield strength of a given material.

A previous forging study proposed that carbon and low-alloy alloys could be easily forged when the temperature was approximately 1123 – 1423 K [39]. At a low temperature, the *HEL* of Q460 steel is high, and the laser shock pressure of the laser forging process is too low to cause plastic deformation of the repaired layer. As shown in **Fig. 15(b)** and in **Table. 5**, the temperature range of the laser forging region is 1105 K ~ 1559 K, which is 62.5% ~ 88.2% of the melting point; the *HEL* is low. In the laser forging region, the laser shock pressure was much higher than the *HEL* of the material, causing plastic deformation of the repaired layer.

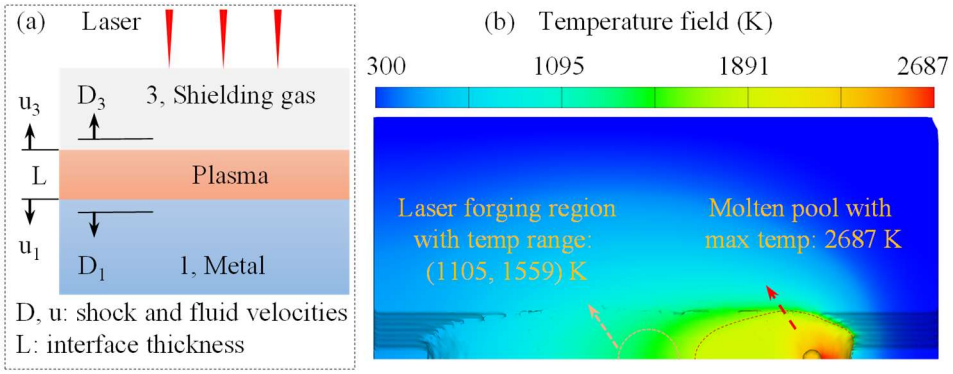

Fig. 15 (a) Geometry of the target assembly in the hybrid process; (b) Calculated temperature field

Table.5 Mechanical properties of Q460 steel

Temp/ K	Possion's ratio	Elastic modulus/ Gpa	Yield strength/ MPa	*HEL*/ MPa
773	0.29	175	300	507.1
1073	0.32	155	17	32.1
1273	0.34	120	13	26.8
1473	0.33	85	13	25.6

Under the impact of laser forging, the solidified primary austenite was subjected to compressive strain to generate compressive deformation and stress. Compared with the unforged austenite, the stability of the forged phase increased, and the C curve shifted to the right, as shown in **Fig. 16**. Therefore, the cooling curve of the unforged repaired layer intersects the bainite transformation range, and the microstructure after cooling is dominated by bainitic ferrite. For the repaired layer after forging,

its C curve is shifted to the right; therefore, its cooling curve directly intersects with the martensite transformation temperature range, resulting in a martensite-based structure.

The high strain and severe plastic deformation induced by laser forging lead to a grain boundary break and increase the dislocation generation, motion, and pile-up. Consequently, high-density dislocations and subcrystal boundaries form inside the surface layer, and the grains of the repaired layer can be refined [40]. Based on the Hall – Patch equation, laser forging increases the tensile strength of the repaired layer through grain refinement. In addition, the martensite-based structure induced by laser forging contributed to the increase in the tensile strength. As the grains are refined, the electrochemical corrosion performance of the forged repaired layer improves.

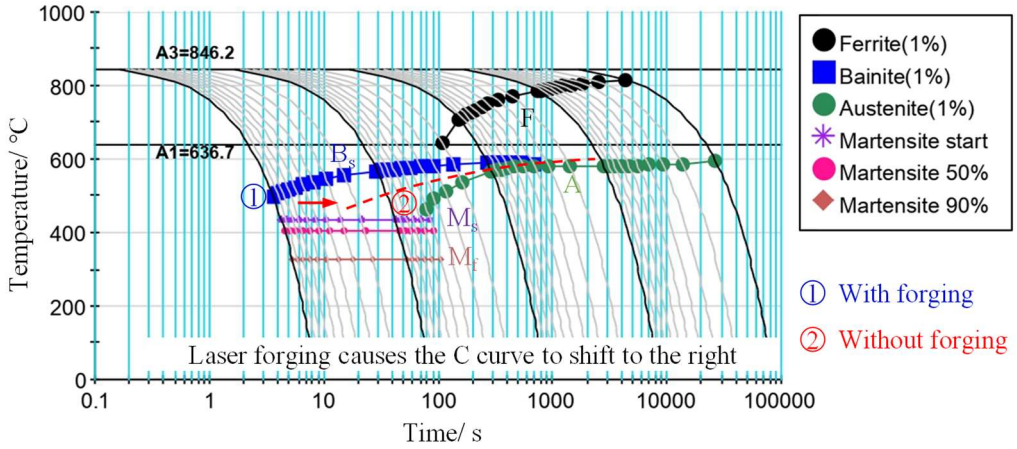

Fig. 16 Continuous cooling transformation (CCT) phase diagram of the repaired layer

5.3 Advantages of the hybrid laser forging and arc additive repairing process

Compared with the hybrid laser directed energy deposition and shot peening process [21], the hybrid laser forging and arc additive repair process can significantly improve both the tensile strength and elongation of the repaired layer, as well as the electrochemical corrosion performance. As plastic deformation of the high-temperature solidified metal easily occurs, a relatively low laser power can be adopted. In previous laser peening studies, the laser power was usually several joules, or more than 10 joules. The laser power used in this study is only 1J, which is much lower than laser peening cases [11,12,17]. The laser forging region can be determined using a multi-physical CFD simulation. Absorbing and confining layers are not necessary; therefore, this novel process is easy to operate. This new hybrid repair process could significantly extend the lifetime of the components used in aerospace, marine, petrochemical, rail transit, and wind power industries, and reduce the manufacturing cost.

6 Conclusions

We developed a new hybrid laser forging and arc additive repair process, in which the arc repair and laser forging were performed synchronously. The molten pool behavior, laser forging mechanism and its effects on the performance of the repaired layer are revealed. The following conclusions were

drawn:

(1) The laser forging region can be accurately determined using a multi-physical CFD simulation considering the complicated molten metal flow. The high sulfur content introduced by filler metal transfer has a significant influence on the Marangoni stress distribution, causing forward/inward flow at the edge of the molten pool.

(2) The mechanism for laser forging without coating is revealed. In the high-temperature laser-forging region, the Hugonoit elastic limit of the material is low. The laser shock pressure was much higher than the Hugonoit elastic limit of the material, causing plastic deformation of the repaired layer.

(3) The high strain and severe plastic deformation induced by laser forging resulted in martensite formation and grain refinement in the repaired layer. The tensile strength and elongation of the repaired layer as well as the electrochemical corrosion performance were significantly improved.

The hybrid laser forging and arc additive repair is a promising process to improve the repair quality and efficiency. In the future research work, we will investigate the influence of laser forging on the residual stress distribution of the repaired layer. We will also try to use an oscillating short-pulse laser to improve the performance of both the fusion zone and heat-affected zone.

Acknowledgments

This research is partially supported by National Nature Science Foundation of China (No. 52105324), AMADA project (AF-2021235-C2), the Science and Technology Planning Project of Jiangsu Province of China (BE2019081).

Reference

[1] Dong, X., Li, N., Zhou, Y., Peng, H., Qu, Y., Sun, Q., Shi, H., Li, R., Xu, S., & Yan, J. (2021). Grain boundary character and stress corrosion cracking behavior of Co-Cr alloy fabricated by selective laser melting. Journal of Materials Science & Technology, 93, 244-253.

[2] Rezaei, M., Mahidashti, Z., Eftekhari, S., & Abdi, E. (2021). A corrosion failure analysis of heat exchanger tubes operating in petrochemical refinery. Engineering Failure Analysis, 119, 105011.

[3] Du, S., Liu, H., Jiang, M., Zhou, L, & Gao, F. (2022). The performance of a Co-based alloy tool in the friction stir welding of TA5 alloy. Wear, 488, 204180.

[4] Barbosa, L. H. S., Modenesi, P. J., Godefroid, L. B., & Arias, A. R. (2019). Fatigue crack growth rates on the weld metal of high heat input submerged arc welding. International Journal of Fatigue, 119, 43-51.

[5] Vishnukumar, M., Pramod, R., & Kannan, A. R. (2021). Wire arc additive manufacturing for repairing aluminium structures in marine applications. Materials Letters, 299, 130112.

[6] Zhuo, Y., Yang, C., Fan, C., & Lin, S. (2022). Effect of diameter and content of zirconium dioxide

on the microstructure and mechanical properties of the TC17 titanium alloy repaired by wire arc additive manufacture. Journal of Alloys and Compounds, 893, 162295.
[7] Xu, K., Qiao, G. Y., Shi, X. B., & Xiao, F. R. (2021). Effect of stress-relief annealing on the fatigue properties of X80 welded pipes. Materials Science and Engineering: A, 807, 140854.
[8] Hao, K., Gao, M., Zhang, C., Wu, R., & Zeng, X. (2019). Cold-rolling performance of non-equilibrium martensitic stainless steel produced by laser-arc hybrid welding. Journal of Materials Processing Technology, 267, 359-365.
[9] Khajeian, A., Mahmoudi, A. H., & Mehmanparast, A. (2019). Shot peening effects on residual stresses redistribution of offshore wind monopile multi-pass weldments. Marine Structures, 66, 106-120.
[10] Lu, J., Lu, H., Xu, X., Yao, J., Cai, J., & Luo, K. (2020). High-performance integrated additive manufacturing with laser shock peening–induced microstructural evolution and improvement in mechanical properties of Ti6Al4V alloy components. International Journal of Machine Tools and Manufacture, 148, 103475.
[11] Wang, C., Luo, K., Wang, J., & Lu, J. (2022). Carbide-facilitated nanocrystallization of martensitic laths and carbide deformation in AISI 420 stainless steel during laser shock peening. International Journal of Plasticity, 150, 103191.
[12] Chin, K. S., Idapalapati, S., & Ardi, D. T. (2020). Thermal stress relaxation in shot peened and laser peened nickel-based superalloy. Journal of Materials Science & Technology, 59, 100-106.
[13] Zhang, Y. K., Lu, J. Z., & Luo, K. Y. (2013). Laser shock processing of FCC metals. Springer Berlin Heidelberg.
[14] Lu, J.Z., Luo, K.Y., Zhang, Y.K., Cui, C.Y., Sun, G.F., Zhou, J.Z., Zhang, L., You, J., Chen, K.M, & Zhong, J.W. (2010). Grain refinement of LY2 aluminum alloy induced by ultra-high plastic strain during multiple laser shock processing impacts. Acta Materialia, 58(11), 3984-3994.
[15] Wei, X. L., & Ling, X. (2014). Numerical modeling of residual stress induced by laser shock processing. Applied surface science, 301, 557-563.
[16] Chattopadhyay, A., Muvvala, G., Sarkar, S., Racherla, V., & Nath, A. K. (2021). Effect of laser shock peening on microstructural, mechanical and corrosion properties of laser beam welded commercially pure titanium. Optics & Laser Technology, 133, 106527.
[17] Chen, X., Wang, J., Fang, Y., Madigan, B., Xu, G., & Zhou, J. (2014). Investigation of microstructures and residual stresses in laser peened Incoloy 800H weldments. Optics & Laser Technology, 57, 159-164.
[18] Kalentics, N., Sohrabi, N., Tabasi, H.G., Griffiths, S., Jhabvala, J., Leinenbach, C., Burn, A, & Loge, R.E. E. (2019). Healing cracks in selective laser melting by 3D laser shock peening. Additive Manufacturing, 30, 100881.

[19] Kalentics, N., de Seijas, M. O. V., Griffiths, S., Leinenbach, C., & Loge, R. E. (2020). 3D laser shock peening–A new method for improving fatigue properties of selective laser melted parts. Additive Manufacturing, 33, 101112.
[20] Pragana, J. P. M., Sampaio, R. F., Bragança, I. M. F., Silva, C. M. A., & Martins, P. A. F. (2021). Hybrid metal additive manufacturing: A state–of–the-art review. Advances in Industrial and Manufacturing Engineering, 2, 100032.
[21] Zhang, X., Huang, S., Li, D., Geng, J., Yang, F., & Li, Q. (2022). An approach to improve the microstructure and mechanical properties: A hybrid manufacturing of laser directed energy deposition and shot peening. Additive Manufacturing, 55, 102686.
[22] Wu, D., Tashiro, S., Wu, Z., Nomura, K., Hua, X., & Tanaka, M. (2020). Analysis of heat transfer and material flow in hybrid KPAW-GMAW process based on the novel three dimensional CFD simulation. International Journal of Heat and Mass Transfer, 147, 118921.
[23] Cho, W. I., Na, S. J., Cho, M. H., & Lee, J. S. (2010). Numerical study of alloying element distribution in CO2 laser–GMA hybrid welding. Computational Materials Science, 49(4), 792-800.
[24] Cho, W. I., & Na, S. J. (2021). Impact of driving forces on molten pool in gas metal arc welding. Welding in the World, 65(9), 1735-1747.
[25] Joseph, A., Harwig, D., Farson, D. F., & Richardson, R. (2003). Measurement and calculation of arc power and heat transfer efficiency in pulsed gas metal arc welding. Science and Technology of Welding & Joining, 8(6), 400-406.
[26] Pépe, N., Egerland, S., Colegrove, P. A., Yapp, D., Leonhartsberger, A., & Scotti, A. (2011). Measuring the process efficiency of controlled gas metal arc welding processes. Science and Technology of Welding and Joining, 16(5), 412-417.
[27] Sun, Z., Guo, W., & Li, L. (2020). Numerical modelling of heat transfer, mass transport and microstructure formation in a high deposition rate laser directed energy deposition process. Additive Manufacturing, 33, 101175.
[28] Zhu, C., Cheon, J., Tang, X., Na, S. J., & Cui, H. (2018). Molten pool behaviors and their influences on welding defects in narrow gap GMAW of 5083 Al-alloy. International Journal of Heat and Mass Transfer, 126, 1206-1221.
[29] Xu, G., Pan, H., Liu, P., Li, P., Hu, Q., & Du, B. (2018). Finite element analysis of residual stress in hybrid laser-arc welding for butt joint of 12 mm-thick steel plate. Welding in the World, 62(2), 289-300.
[30] Zhou, X., Zhang, H., Wang, G., & Bai, X. (2016). Three-dimensional numerical simulation of arc and metal transport in arc welding based additive manufacturing. International Journal of Heat and Mass Transfer, 103, 521-537.
[31] Zong, R., Chen, J., & Wu, C. (2020). A comparison of double shielded GMAW-P with

conventional GMAW-P in the arc, droplet and bead formation. Journal of Materials Processing Technology, 285, 116781.
[32] Cho, M. H., Lim, Y. C., & Farson, D. F. (2006). Simulation of weld pool dynamics in the stationary pulsed gas metal arc welding process and final weld shape. Welding Journal, 85(12), 271s-283s.
[33] Aucott, L., Dong, H., Mirihanage, W., Atwood, R., Kidess, A., Gao, S., Wen, S., Marsden, J., Feng, S., Tong, M. & Connolley, T. (2018). Revealing internal flow behaviour in arc welding and additive manufacturing of metals. Nature communications, 9(1), 5414.
[34] Cheon, J., Kiran, D. V., & Na, S. J. (2016). CFD based visualization of the finger shaped evolution in the gas metal arc welding process. International Journal of Heat and Mass Transfer, 97, 1-14.
[35] Liao, Y., Suslov, S., Ye, C., & Cheng, G. J. (2012). The mechanisms of thermal engineered laser shock peening for enhanced fatigue performance. Acta Materialia, 60, 4997-5009.
[36] Wei, X. L., & Ling, X. (2014). Numerical modeling of residual stress induced by laser shock processing. Applied surface science, 301, 557-563.
[37] Fabbro, R., Fournier, J., Ballard, P., Devaux, D., & Virmont, J. (1990). Physical study of laser-produced plasma in confined geometry. Journal of applied physics, 68(2), 775-784.
[38] Kanel, G. I., Razorenov, S. V., Fortov, V. E., & Fortov, V. E. (2004). Shock-wave phenomena and the properties of condensed matter. Springer Science & Business Media.
[39] Altan, T., Ngaile, G., & Shen, G. (2004). Cold and hot forging: fundamentals and applications. ASM international.
[40] Wang, J. T., Zhang, Y. K., Chen, J. F., Zhou, J. Y., Ge, M. Z., Lu, Y. L., & Li, X. L. (2015). Effects of laser shock peening on stress corrosion behavior of 7075 aluminum alloy laser welded joints. Materials Science and Engineering: A, 647, 7-14.